Dark-Field Signal Retrieval Using Single-Mask Edge-Illumination X-ray Imaging

Universidad de los Andes, High Energy Physics Lab

Thomas Andrade Hernández
t.andrade@uniandes.edu.co

June 12 2026

Presentation Outline

1. Research Motivation
2. Theoretical Framework
3. Acquisition Methods
4. Future Work
5. Remarks
6. References

Transmission, Refraction and Scattering Signals

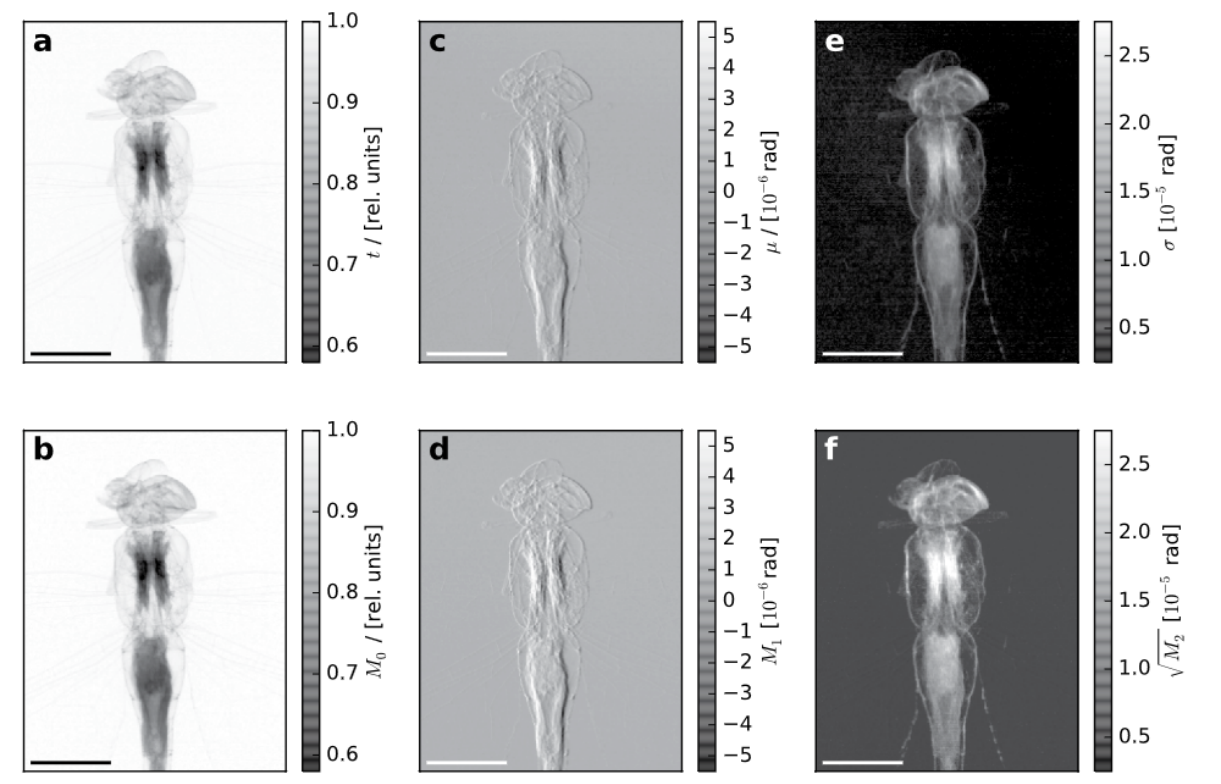

Figure: Contrast signals retrieved from a dragon fly. Each column represents transmission T (a, b), refraction $\nabla_\perp \phi$ (c, d) and scattering σ^2 (e, f). The difference between each row is the application of a de-convolution process. Figure reproduced from [1].

Transport of Intensity Equation

The propagation of light through an imaging system can be decomposed into different contributions using the Fokker-Planck extension of the Transport of Intensity Equation [2, 3] (TIE):

$$I(\vec{r}, z) - I(\vec{r}, 0) = \underbrace{z\nabla_\perp^2 \left[S(\vec{r})I(\vec{r}, 0)\right]}_{\text{Diffusive}} \underbrace{-\frac{z}{k}\nabla_\perp \cdot \left[I(\vec{r}, 0)\nabla_\perp \phi(\vec{r}, 0)\right]}_{\text{Coherent}} \tag{1}$$

Here, $S(\vec{r})$ denotes the effective scattering coefficient, and $\nabla_\perp = (\partial_x, \partial_y)$ is the transverse gradient operator acting only in the xy plane.

Transport of Intensity Equation

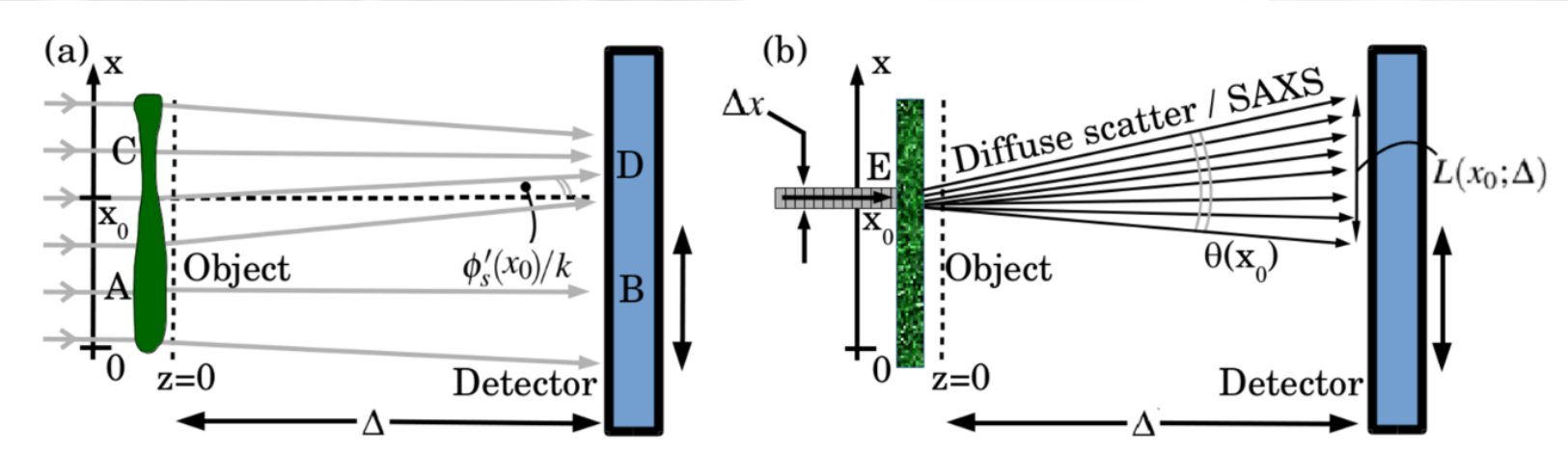

Figure: Physical representation of the two terms in the Fokker-Planck TIE. (a) Coherent transport: specular refraction locally redistributes the photon energy density, giving rise to the differential phase-contrast signal. (b) Diffusive transport: ultra-small-angle X-ray scattering (USAXS) spreads energy into a narrow forward cone, giving rise to the dark-field signal. Figure adapted from [2].

The Dark Field Signal

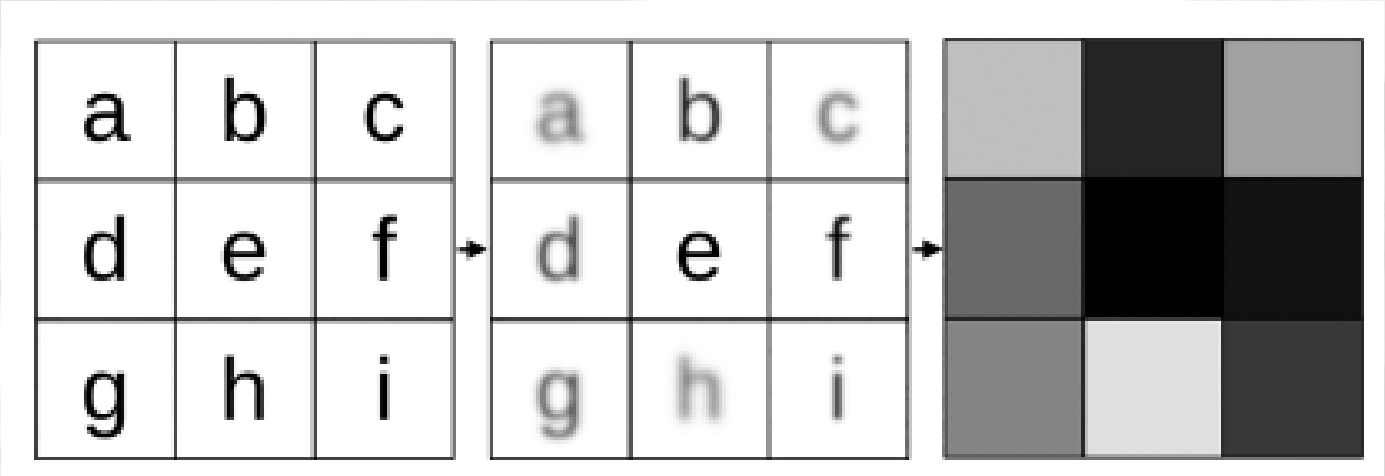

Figure: The dark-field signal arises from USAXS produced by sub-pixel microstructures. Scattering locally redistributes photon energy, causing uniform blurring within the scattering region that is invisible to both attenuation and phase contrast imaging. FFigure reproduced from [4].

Single-mask Edge Illumination

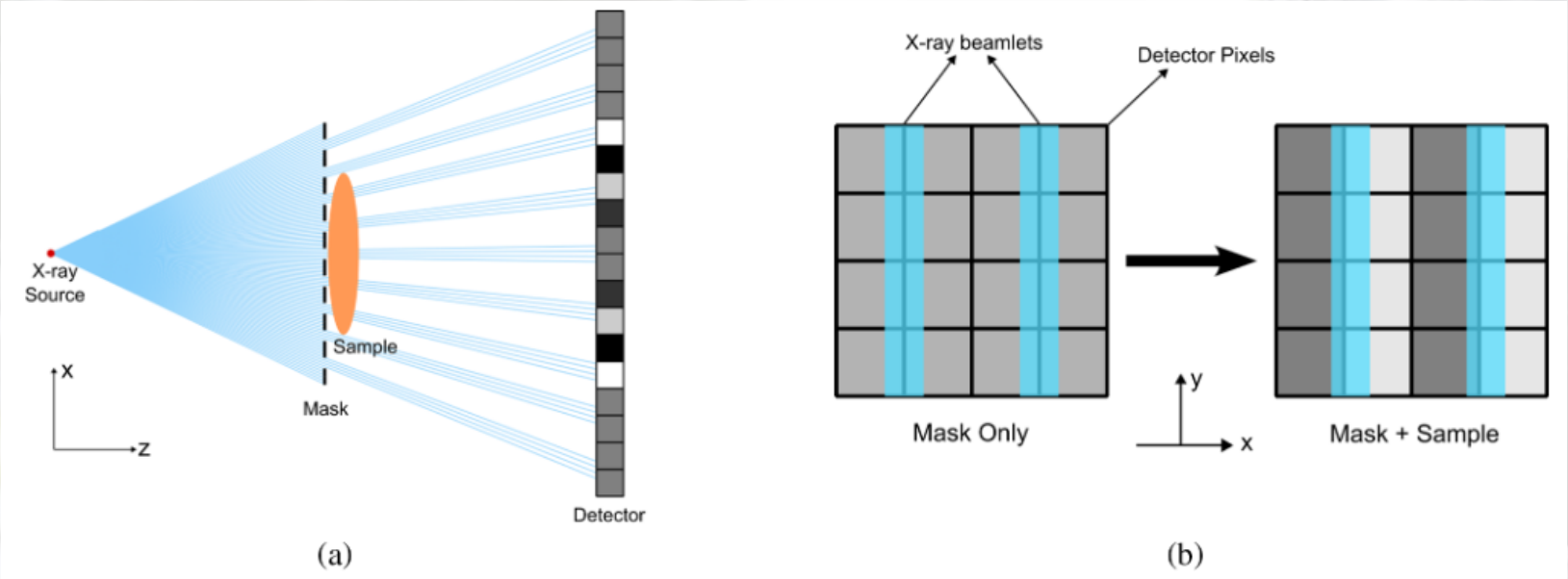

Figure: (a) SM-EI XPCI setup schematic, (b) illustrates the edge-illumination condition for the single-mask modality, as only the border between consecutive pixels must be illuminated to be able to use the SM-EI formalism. Figure reproduced from [3].

Single-mask Edge Illumination

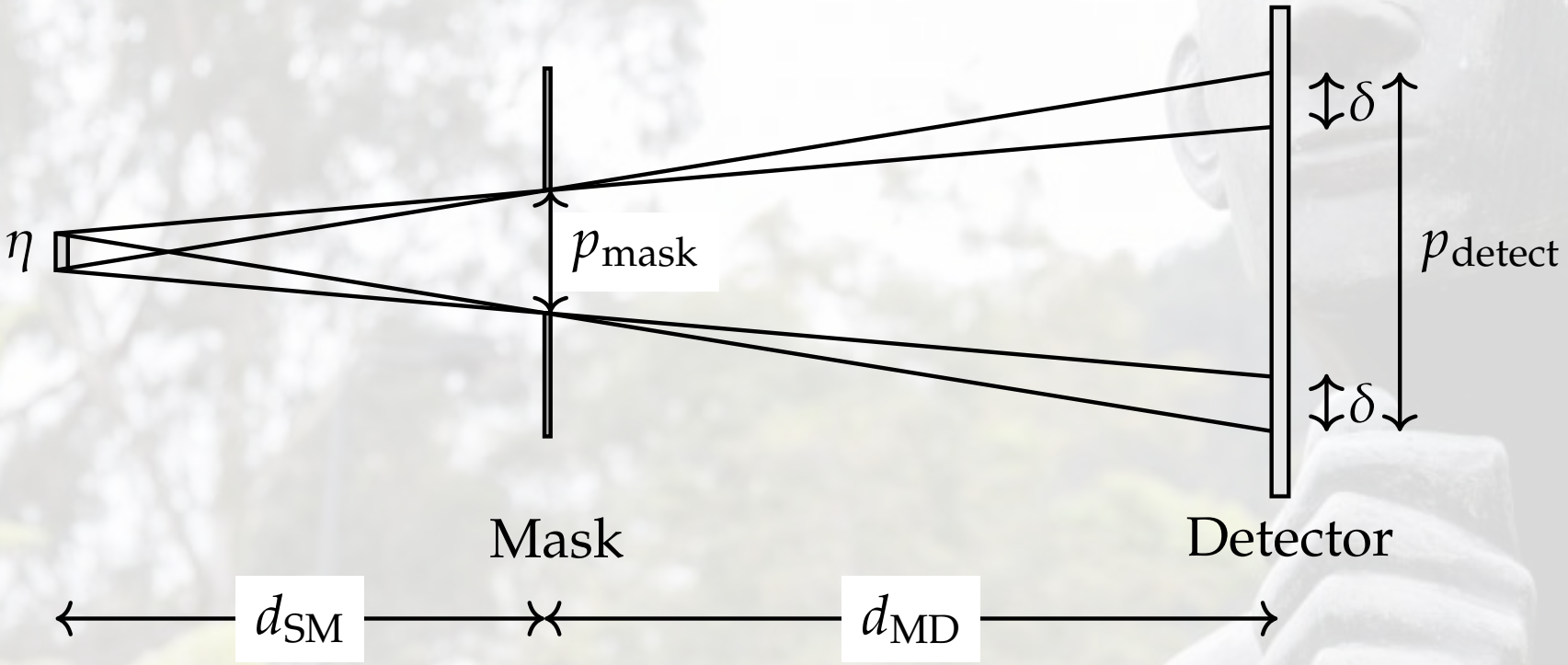

Beam Tracking by Chang Li *et al.* (2026)

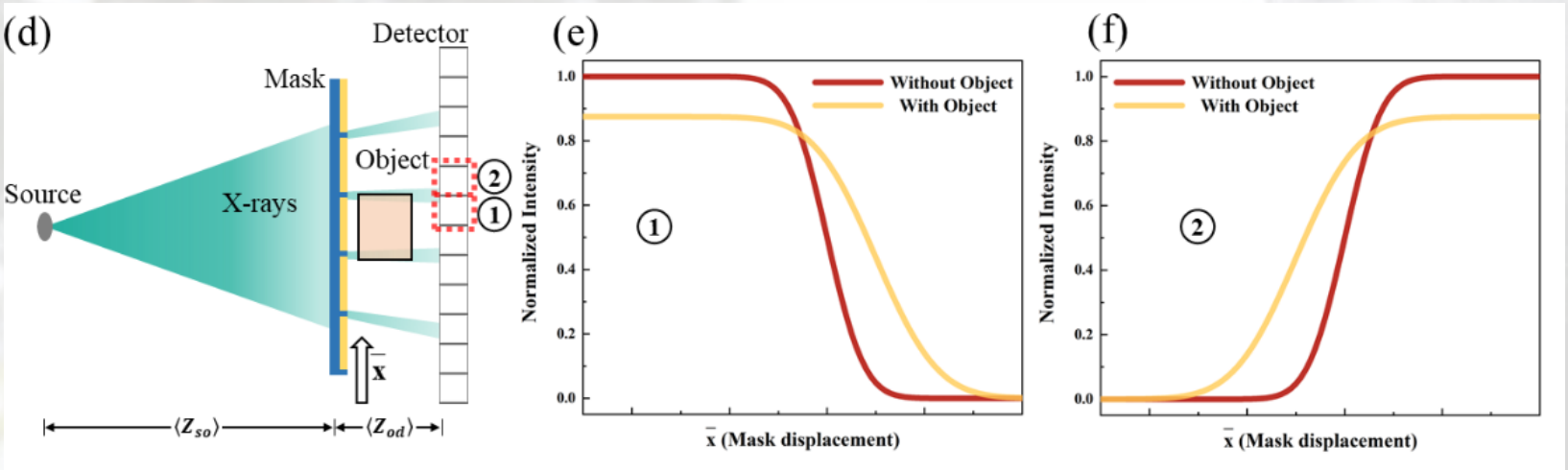

Figure: SM EI setup used by Chang Li *et al.* with large detection pixels and low system magnification. The illumination curve (IC) for each pixel exhibits a sigmoid shape, whose parameters encode absorption, refraction and scattering. (e) and (f) show the changes in SM ICs for pixels (1) and (2) in (d) without and with the sample, respectively. Figure reproduced from [5].

Beam Tracking by Chang Li *et al.* (2026)

Each pixel intensity curve can be modeled as:

$$I(\bar{x}, A_g, \mu_g, \sigma_g^2) = \frac{A_g}{2}\left[\mathrm{erf}\left(\frac{x-\mu_g}{\sqrt{2\sigma_g^2}}\right) + \mathrm{erf}\left(\frac{3\sigma_g}{\sqrt{2\sigma_g^2}}\right)\right] + \text{Constant} \quad (2)$$

The contrast signals can be retrieved using:

$$\mu = -\ln\left(\frac{A_{g,1}}{A_{g,0}}\right) \quad (3)$$

$$\Delta\theta_x = \frac{M\left(\mu_{g,1} - \mu_{g,0}\right)}{z_{\mathrm{od}}} \quad (4)$$

$$\sigma_\Phi^2 = \frac{M^2\left(\sigma_{g,1}^2 - \sigma_{g,0}^2\right)}{z_{\mathrm{od}}^2} \quad (5)$$

Beam Tracking by Chang Li *et al.* (2026)

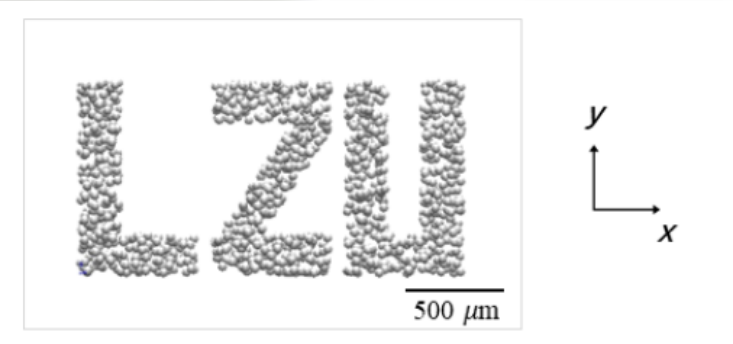

Figure: Scattering sample used to test the beam tracking approach. The spheres are made of graphite and have a diameter of 50μm. The pixel size of the detector is 62μm $\times$ 62μm and the z_{so} = 80cm and z_{od} = 20cm (M = 1.25). Figure taken from [5].

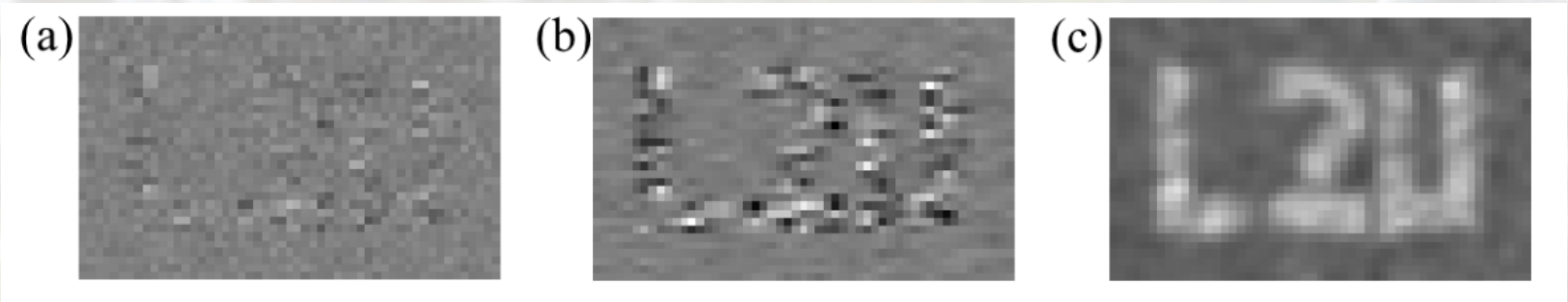

Figure: Retrieved absorption (a), refraction (b) and scattering (c) signals. Figure taken from [5].

Mask Alignment by Yuan and Das (2025)

By modelling the beam intensity after interacting with the sample as [6]:

$$I(\vec{r}, 0) = T(\vec{r}) \cdot M(x) \tag{6}$$

with $T(\vec{r})$ and $M(x)$ denoting the object and mask transmission functions, respectively, and modeling the latter as

$$M(x) = \sum_{m=0}^{\infty} C_m \cos\left(\frac{2\pi m}{p_{\text{Mask}}} x + \delta_{\text{align}}\right) \tag{7}$$

Yuan and Das developed a method capable of estimating the different contrast channels by only using different masks and mask alignments.

$$\begin{aligned} I_n = {} & T(x_n) \int_{x_n}^{x_{n+1}} M(x)\, dx - \frac{z}{k} T(x_n) \nabla_\perp^2 \phi(x_n) \int_{x_n}^{x_{n+1}} M(x)\, dx \\ & - \frac{z}{k} T(x_n) \partial_x \phi(x_n) \int_{x_n}^{x_{n+1}} M'(x)\, dx + z T(x_n) S(x_n) \int_{x_n}^{x_{n+1}} M''(x)\, dx \end{aligned} \tag{8}$$

Mask Alignment by Yuan and Das (2025)

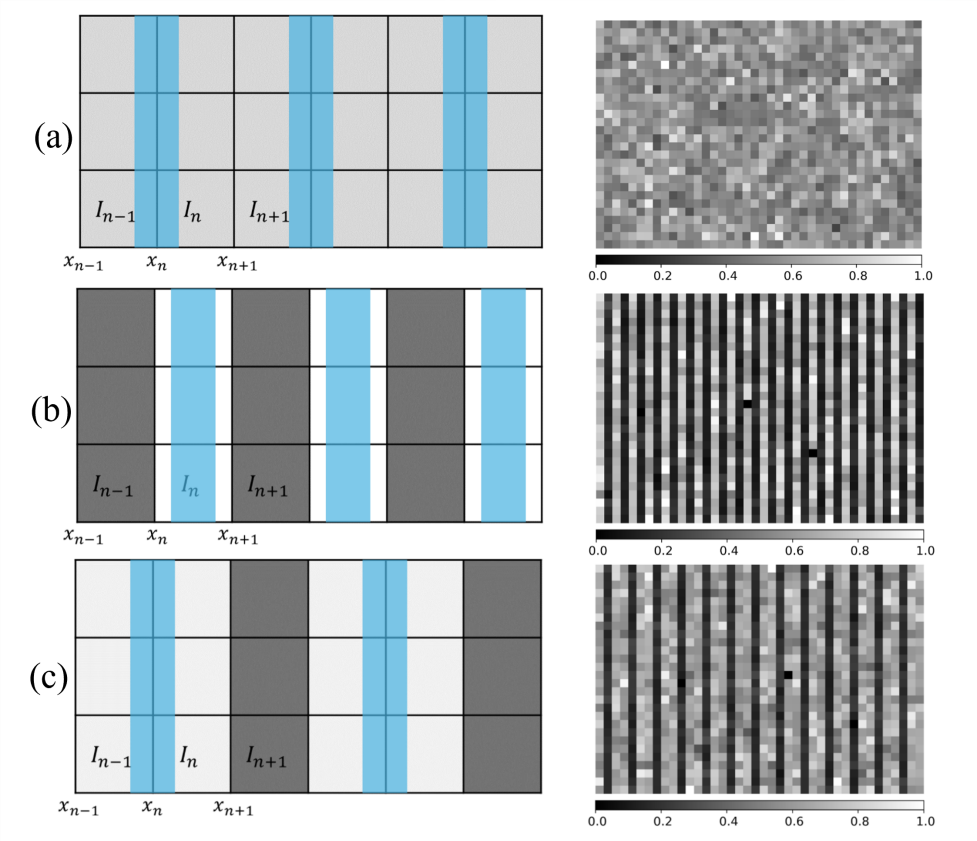

Figure: Mask alignment configurations for contrast retrieval: (a) attenuation and differential phase, (b) attenuation and dark-field, and (c) simultaneous retrieval of all contrast channels. Figure adapted from [6].

Mask Alignment by Yuan and Das (2025)

Single-mask DPC configuration:

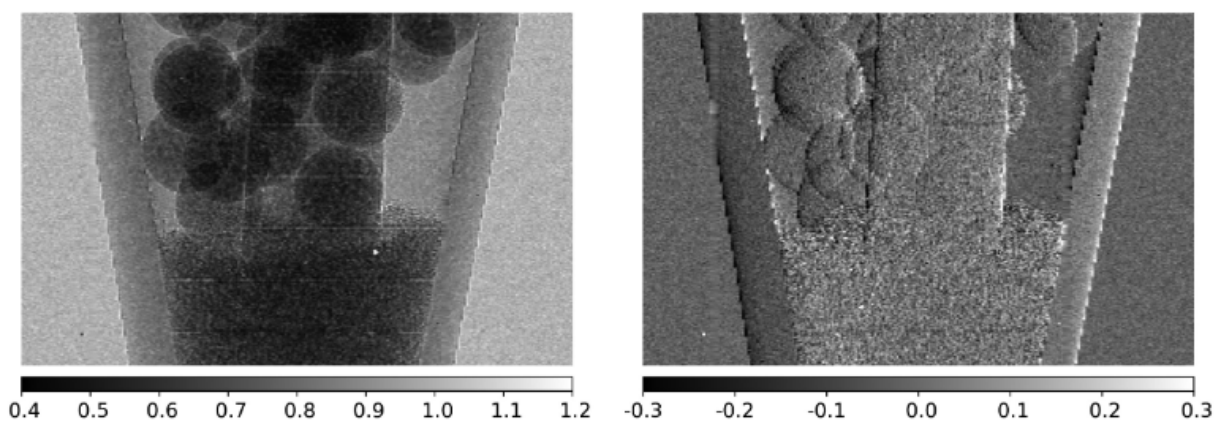

Figure: Retrieved attenuation (left) and differential phase (right) signals for a multimaterial sample. Figure adapted from [6].

$$\begin{cases} T_n(1 - L_n) = \dfrac{\bar{I}_n + \bar{I}_{n+1}}{2} \\ \dfrac{\alpha}{w_e} D_n = \dfrac{\bar{I}_n - \bar{I}_{n+1}}{\bar{I}_n + \bar{I}_{n+1}} \end{cases}$$

Mask Alignment by Yuan and Das (2025)

Single-mask DF configuration:

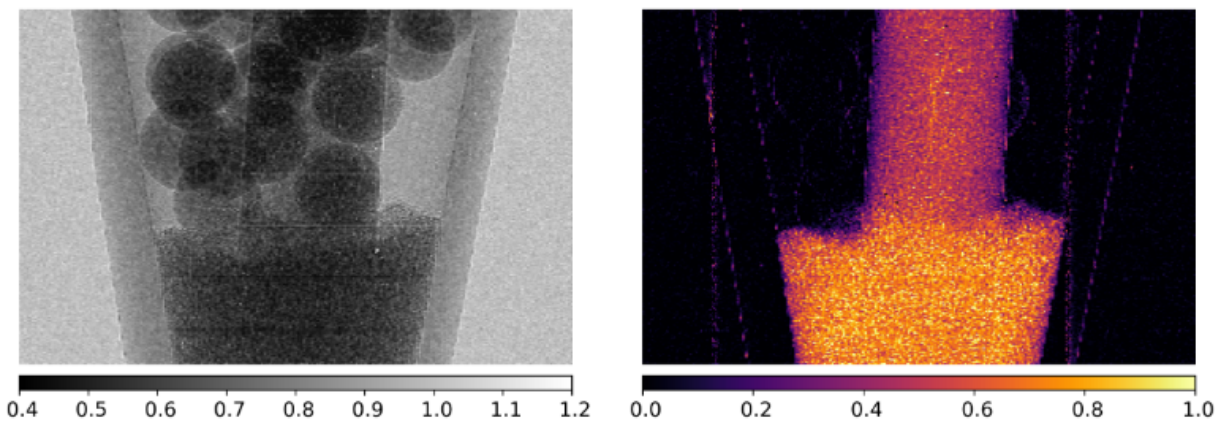

Figure: Retrieved attenuation (left) and dark-field (right) signals for a multimaterial sample. Figure adapted from [6].

$$\begin{cases} T_n(1-L_n) = \dfrac{I_n^{(S)} + I_{n+1}^{(S)}}{I_n^{(M)} + I_{n+1}^{(M)}} \\ \dfrac{\alpha_3}{\alpha_1} S_n = 1 - \dfrac{I_n^{(S)} - I_{n+1}^{(S)}}{I_n^{(M)} - I_{n+1}^{(M)}} \cdot \dfrac{I_n^{(M)} + I_{n+1}^{(M)}}{I_n^{(S)} + I_{n+1}^{(S)}} \end{cases}$$

Mask Alignment by Yuan and Das (2025)

Single-mask DF-DPC configuration:

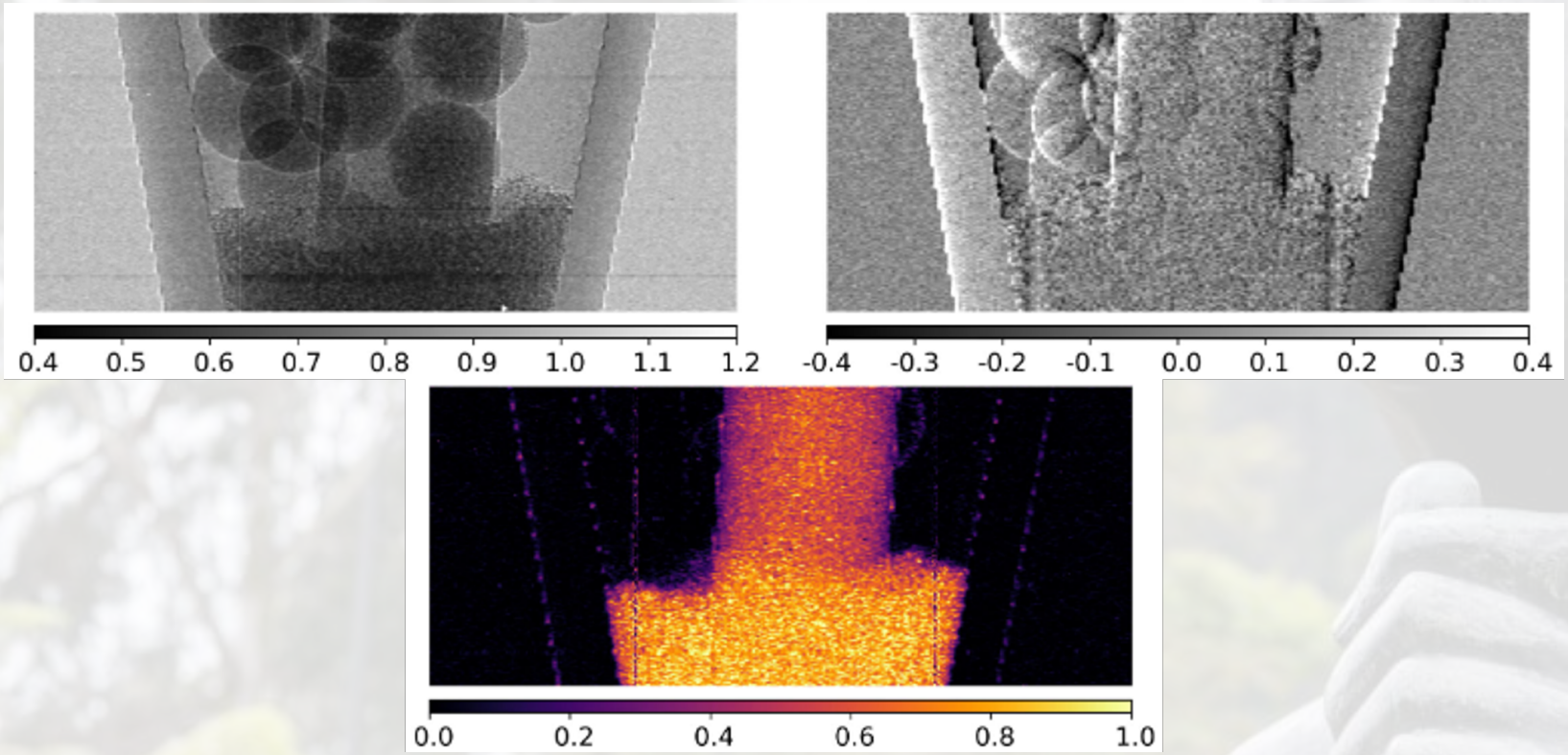

Figure: Retrieved attenuation (left), differential phase (right) and dark-field (down) signals for a multimaterial sample. Figure adapted from [6].

Mask Alignment by Yuan and Das (2025)

The DF-DPC configuration recovers all three contrast channels simultaneously from adjacent pixel triplets in a single exposure:

$$
\begin{cases}
T_n(1 - L_n) = \dfrac{I_{n-1}^{(S)} + I_n^{(S)} + I_{n+1}^{(S)}}{I_{n-1}^{(M)} + I_n^{(M)} + I_{n+1}^{(M)}} \\
\dfrac{2\alpha_2}{w_e + \frac{1}{2}\alpha_1} D_n = \left(\dfrac{I_{n-1}^{(S)}}{I_{n-1}^{(M)}} - \dfrac{I_n^{(S)}}{I_n^{(M)}} \right) \dfrac{I_{n-1}^{(M)} + I_n^{(M)} + I_{n+1}^{(M)}}{I_{n-1}^{(S)} + I_n^{(S)} + I_{n+1}^{(S)}} \\
\dfrac{\alpha_3}{\alpha_1} S_n = \left[1 - \dfrac{I_{n-1}^{(S)} + I_n^{(S)} - 2I_{n+1}^{(S)}}{I_{n-1}^{(M)} + I_n^{(M)} - 2I_{n+1}^{(M)}} \cdot \dfrac{I_{n-1}^{(M)} + I_n^{(M)} + I_{n+1}^{(M)}}{I_{n-1}^{(S)} + I_n^{(S)} + I_{n+1}^{(S)}} \right]
\end{cases}
$$

Mask Alignment by Yuan and Das (2025)

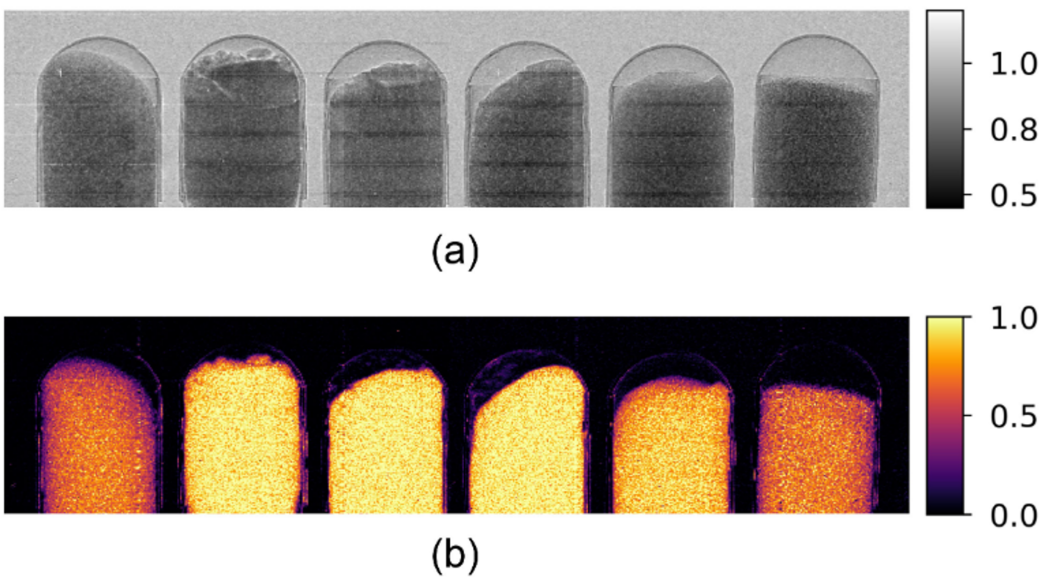

Table 1. Approximate Grain Size of Each Diamond Powder Sample

Sample Number	1	2	3	4	5	6
Grain size (μm)	0–0.25	0–0.5	0–1	2–3	10–20	50–80

Figure: Retrieved (a) attenuation image and (b) dark-field image of six capsules filled with diamond powders of different grain sizes. From left to right corresponds to the sample numbers 1-6 in Table 1. Figure reproduced from [6].

Limitations and Open Questions

Chang Li *et al.* limitations:

- Requires multiple exposures, which increases the radiation dose received by the sample.
- All of the signals depend on accurately fitting the intensity curve at each pixel.

Yuan and Das limitations:

- Spatial resolution is heavily decreased, each method halves (DPC and DF) or reduces by a factor of three (DF-DPC) the effective pixels of the detector.

None of these methods use the energy dependence of the dark-field signal.

The Energy Dependence of the Dark-field Signal

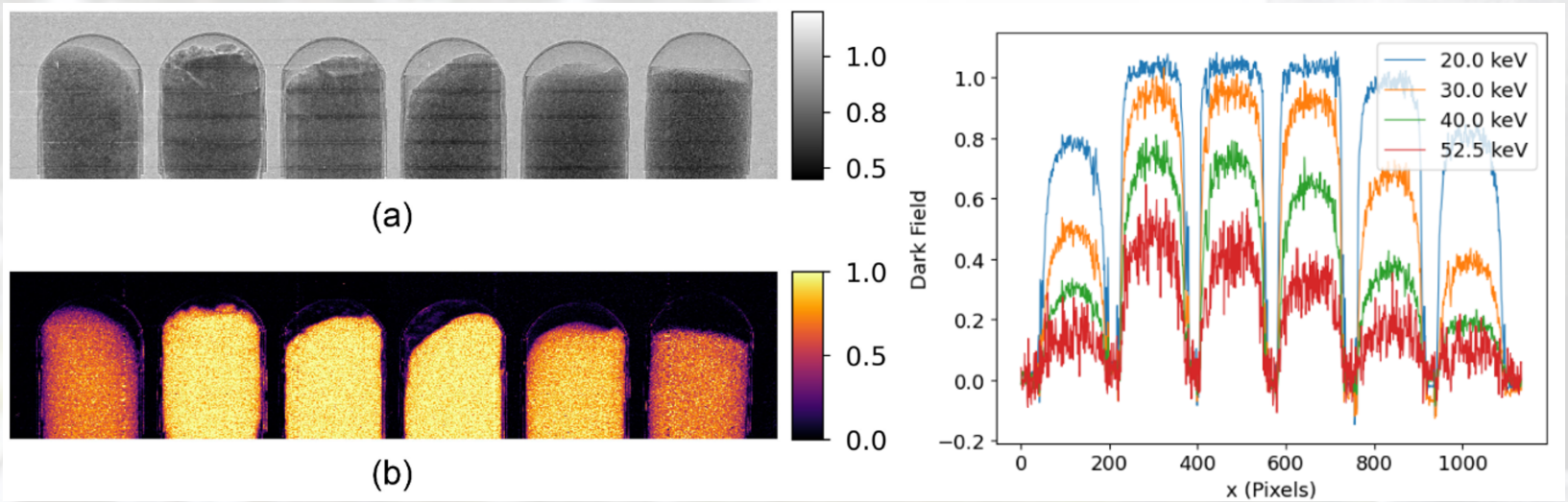

Figure: Retrieved (a) attenuation image and (b) dark-field image of six capsules filled with diamond powders of different grain sizes. The graph on the left shows the horizontal profiles at different energies. Figure adapted from [6].

The Energy Dependence of the Dark-field Signal

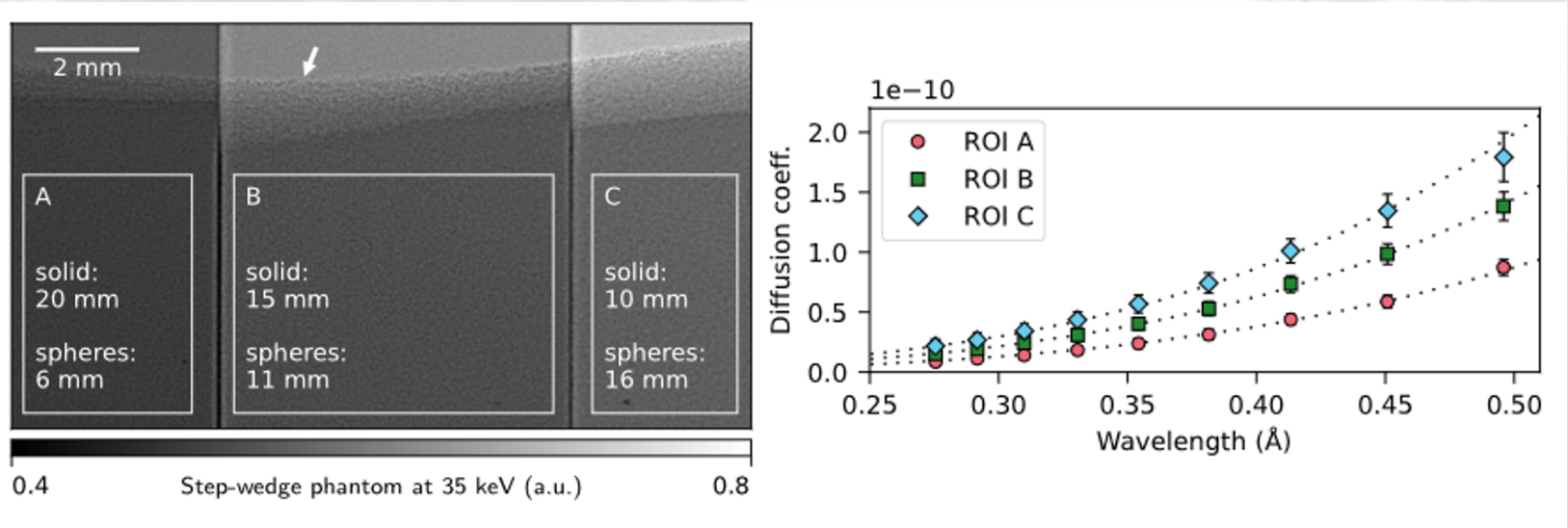

Figure: (Left)Image of a wedge-shaped PMMA phantom with a voided region containing PMMA microspheres with diameters of $45 - 53\mu$m. (Right) Mean diffusion coefficient of the wedge-shaped phantom. The results were fitted with a power-law model $D_i(\lambda) = a_i\lambda^b$, where λ is the wavelength, i indexes the different regions, and a_i and b are free parameters. The estimated exponent was found to be $b = 3.72 \pm 0.03$. Figure adapted from [7].

An Energy Based Optimization Method

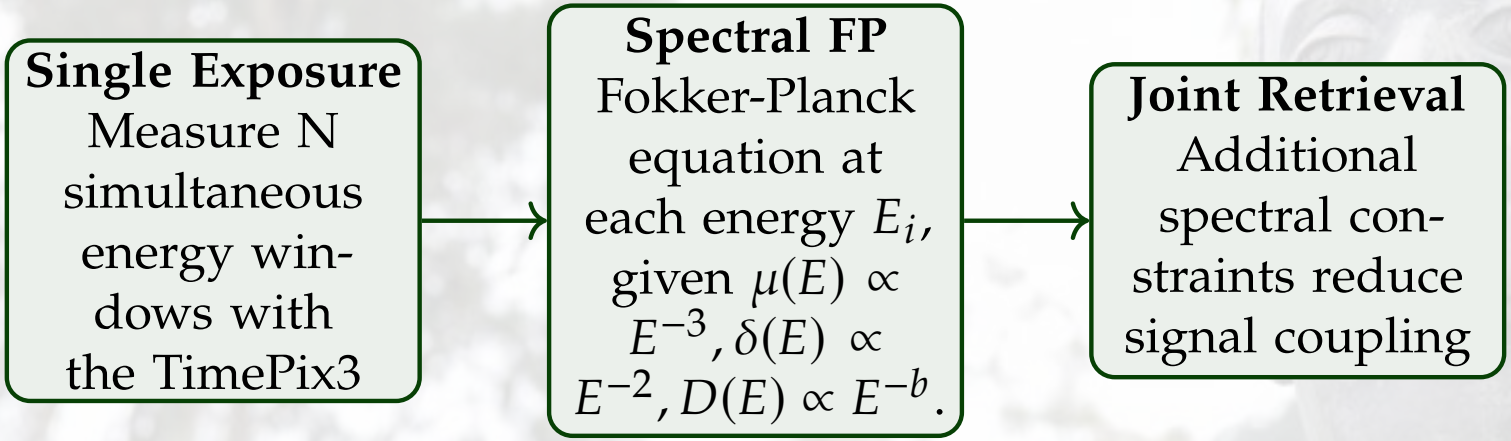

Research Hypothesis

The distinct energy dependence of absorption, refraction, and dark-field signals may allow their separation through spectral analysis.

All of this will be validated through Geant4/PEPILab simulations and TimePix3 measurements.

Remarks of the Presentation

1. Dark-field imaging reveals sub-pixel microstructures through USAXS, providing complementary information to attenuation and phase contrast that is otherwise inaccessible.
2. Single-mask edge illumination enables single-shot retrieval of all three contrast signals through mask-pixel alignment, without requiring either ultra-high-resolution detectors or multiple exposures.
3. The energy-dependent signatures of absorption, phase and dark-field signals provide a natural route to improve their decoupling through spectral single-mask EI, exploiting photon-counting detectors like the TimePix3.


Thank you for your attention

References

[1] P. Modregger, T. P. Cremona, C. Benarafa, J. C. Schittny, A. Olivo, and M. Endrizzi, "Small angle x-ray scattering with edge-illumination", Scientific Reports **6**, 10.1038/srep30940 (2016).

[2] D. M. Paganin and K. S. Morgan, "X-ray fokker-planck equation for paraxial imaging", Scientific Reports **9**, 10.1038/s41598-019-52284-5 (2019).

[3] J. Yuan and M. Das, "Transport-of-intensity model for single-mask x-ray differential phase contrast imaging", Optica **11**, 478 (2024).

[4] D. M. Paganin, D. Pelliccia, and K. S. Morgan, "Paraxial diffusion-field retrieval", Physical Review A **108**, 10.1103/physreva.108.013517 (2023).

[5] C. Li, L. Lv, X. Ren, Y. Lei, X. Pan, C. Zhang, and G. Li, "Large-size multi-contrast imaging technology based on single-mask edge illumination: concept and simulation", Journal of Instrumentation **21**, P03001 (2026).

[6] J. Yuan and M. Das, "Single-shot, single-mask x-ray dark-field, and phase-contrast imaging", Optica **12**, 1895 (2025).

[7] J. N. Ahlers, K. M. Pavlov, M. J. Kitchen, and K. S. Morgan, "X-ray dark-field via spectral propagation-based imaging", Optica **11**, 1182 (2024).